Volume 9
Number 4
April 2022
Pages 1101–1320

Materials Horizons

rsc.li/materials-horizons

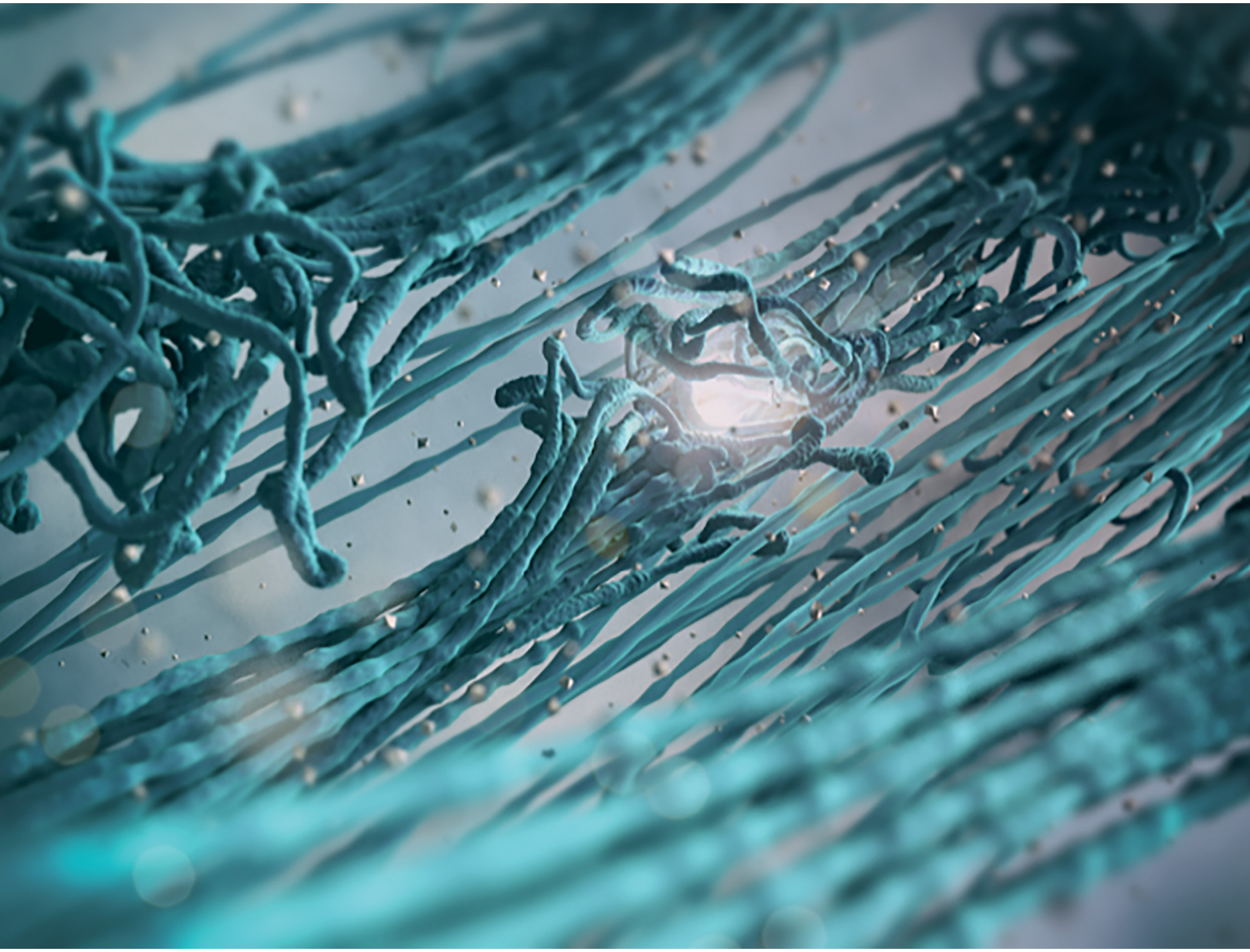

ISSN 2051-6347

ROYAL SOCIETY OF **CHEMISTRY**

COMMUNICATION
Harald Ade, Jaime Martin *et al.*
Semi-paracrystallinity in semi-conducting polymers

Materials
Horizons

ROYAL SOCIETY
OF CHEMISTRY

COMMUNICATION

View Article Online
View Journal | View Issue

Check for updates

Cite this: *Mater. Horiz.*, 2022, 9, 1196

Received 20th August 2021,
Accepted 14th December 2021

DOI: 10.1039/d1mh01349a

rsc.li/materials-horizons

Semi-paracrystallinity in semi-conducting polymers†

Sara Marina,[a] Edgar Gutierrez-Fernandez,[a] Junkal Gutierrez,[bc] Marco Gobbi,[def] Nicolás Ramos,[a] Eduardo Solano,[g] Jeromy Rech,[h] Wei You,[h] Luis Hueso,[de] Agnieszka Tercjak,[b] Harald Ade*[i] and Jaime Martin*[ajk]

Precise determination of structural organization of semi-conducting polymers is of paramount importance for the further development of these materials in organic electronic technologies. Yet, prior characterization of some of the best-performing materials for transistor and photovoltaic applications, which are based on polymers with rigid backbones, often resulted in conundrums in which X-ray scattering and microscopy yielded seemingly contradicting results. Here we solve the paradox by introducing a new structural model, *i.e.*, semi-paracrystalline organization. The model establishes that the microstructure of these materials relies on a dense array of small paracrystalline domains embedded in a more disordered matrix. Thus, the overall structural order relies on two parameters: the novel concept of degree of paracrystallinity (*i.e.*, paracrystalline volume/mass fraction, introduced here for the first time) and the lattice distortion parameter of paracrystalline domains (*g*-parameter from X-ray scattering). Structural parameters of the model are correlated with long-range charge carrier transport, revealing that charge transport in semi-paracrystalline materials is particularly sensitive to the interconnection of paracrystalline domains.

New concepts

Based on the study of high-performing semi-conducting polymer thin films, we introduce here a new structural model for polymer materials: the semi-paracrystalline model. This model asserts that semi-conducting polymers are a class of materials where small paracrystalline domains coexists with more disordered regions. The assessment of structural order in semi-paracrystalline materials requires to consider not only the quality of ordering of the paracrystalline lattice (*g*-parameter) but also the degree of paracrystallinity (*i.e.*, paracrystalline volume/mass fraction), which is introduced here for the first time. The new model is able to rationalize the seemingly contradictory data in the literature and allows reliable description of the solid-state microstructure of semi-conducting polymer materials. Furthermore, it allows establishing the interplay between electrical charge transport in semi-conducting polymers and the key structural features of the model.

Introduction

The ability of semi-conducting polymers to transport charges has proven to be closely connected with their solid-state microstructure and, more specifically, with the presence of ordered molecular structures, such as crystals, their characteristics (*i.e.* size, orientation, defects, intrinsic disorder, *etc.*) and the interconnection between them, *e.g. via* tie-chains.[1]

From the solid-state microstructure standpoint, polymeric materials have been typically classified as either amorphous (glassy) or partially crystalline (*i.e.* semi-crystalline) (see Fig. 1).[2] An amorphous polymer material consists of polymer chains adopting disordered coil-like conformations resulting from the enormous number of possible rotational isomeric states of chains. They tend to be glasses and, as such, they exhibit a glass transition temperature, T_g. In partially crystalline

---

[a] *POLYMAT, University of the Basque Country UPV/EHU Av. de Tolosa 72, 20018, Donostia-San Sebastián, Spain*
[b] *Group 'Materials + Technologies', Faculty of Engineering Guipuzcoa, University of the Basque Country (UPV/EHU), Plaza Europa 1, 20018 Donostia, Spain*
[c] *Faculty of Engineering Vitoria-Gasteiz, University of the Basque Country (UPV/EHU), C/Nieves Cano 12, 01006 Vitoria-Gasteiz, Spain*
[d] *CIC nanoGUNE BRTA, 20018 Donostia-San Sebastian, Basque Country, Spain*
[e] *IKERBASQUE, Basque Foundation for Science, 48013 Bilbao, Basque Country, Spain*
[f] *Centro de Física de Materiales CFM-MPC (CSIC-UPV/EHU), 20018 Donostia-San Sebastian, Basque Country, Spain*
[g] *ALBA Synchrotron Light Source, NCD-SWEET Beamline, 08290 Cerdanyola del Vallès, Spain*
[h] *Department of Chemistry, University of North Carolina at Chapel Hill, Chapel Hill, North Carolina, 27599, USA*
[i] *Department of Physics and Organic and Carbon Electronics Laboratories (ORaCEL), North Carolina State University, Raleigh, NC, 27695, USA. E-mail: hwade@ncsu.edu*
[j] *Universidade da Coruña, Grupo de Polímeros, Centro de Investigacións Tecnolóxicas (CIT), Esteiro, 15471 Ferrol, Spain*
[k] *Ikerbasque, Basque Foundation for Science, 48013 Bilbao, Spain. E-mail: jaime.martin.perez@udc.es*

† Electronic supplementary information (ESI) available. See DOI: 10.1039/d1mh01349a

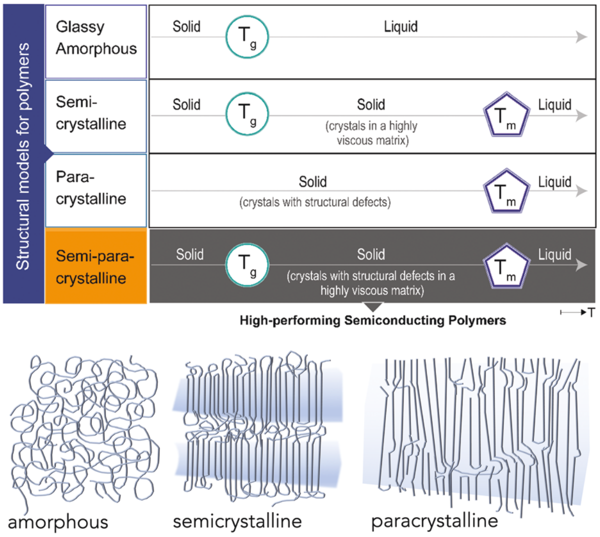

Fig. 1 Structural models for (non-liquid-crystalline) polymers and their relevant temperatures: glass transition temperature, T_g, and order–disorder (melting) temperatures, T_m.

polymers, traditional models, *e.g.* the "fringed micelle model"[3] or the spherulitic model,[4] assume that amorphous regions combine with crystalline regions in which chain segments with relatively extended conformations are stacked in lamellar crystallites.[2,5] Hence, semicrystalline materials exhibit both a T_g and a crystal melting temperature (T_m). Thus, these structural models for semi-crystalline materials allow for a simple parametrization of the overall degree of structural order in terms of the degree of crystallinity, *i.e.* the fraction of crystalline regions to the total volume/mass of the sample. The characteristics of the semi-crystalline microstructure (*e.g.* semi-crystalline morphology and structure parameters) can be inferred from the combination of diffraction techniques (*e.g.* X-ray diffraction), microscopies (optical, electronic and force microscopies), and methods probing the melting of crystals, the most common being differential scanning calorimetry (DSC).[2] Thus, the identification and quantification of structural order in semi-crystalline polymeric materials has been traditionally realized analyzing *e.g.* the Bragg peaks of the X-ray diffraction patterns, measuring the birefringence under a cross-polarized optical microscope (POM), and/or quantifying the enthalpy change during the melting of crystals by DSC. Obviously, amorphous polymer materials do not feature any of the aforementioned signals.

The analysis of solution-spun lyotropic polymers, such as aramid fibers,[6,7] revealed, moreover, a different solid-state order – somehow between that of crystalline and amorphous materials – described by the so-called paracrystalline model (Fig. 1).[8–10] Contrarily to semicrystalline materials, the overall degree of structural order in paracrystalline materials is not given by the volume fraction occupied by structurally ordered and disordered regions, but by the quality of the paracrystalline lattice, *i.e.* the lattice disorder as captured in the paracrystallinity distortion parameter, g (further details about paracrystallinity and the calculation of g are provided in the ESI†).

Progress in materials engineering for organic electronics has led to the development of semiconducting polymers with solid-state microstructures ranging from completely amorphous, *e.g.* poly[bis(4-phenyl)(2,4,6-trimethylphenyl)amine (PTAA),[1] to some with moderate-to-high degrees of structural ordering, *e.g.* poly(3-hexylthiophene-2,5-diyl) (P3HT) and poly[2,5-bis(3-tetradecylthiophen-2-yl)thieno[3,2-*b*]thiophene] (PBTTT).[1,11] The degree of order in these highly-ordered semiconducting polymers can be readily characterized by, *e.g.*, DSC and X-ray methods[12,13] like in commodity semicrystalline polymers. However, the analysis of the quality of the molecular packing in semiconducting polymers revealed that even the most ordered materials feature a fairly disordered π-stacking; *e.g.* g-parameters of 7.3% were measured for PBTTT[14] while those of typical semicrystalline polymers such as poly(ε-caprolactona) (PCL) or poly(vinylidene fluoride (PVDF) amount to 4% and 2%, respectively. Hence, it has been proposed that ordered structural elements in many semi-conducting polymer films exhibit greater similarity with paracrystals than with regular crystals.

But unlike typical paracrystalline materials, such as aramide fibers, semiconducting polymer thin films might contain also significant fractions of structurally disordered regions, resulting in a semi-paracrystalline solid-state microstructure (Fig. 1). Hence, the g-parameter is not sufficient to characterize the overall degree of structural order of these materials, as it is solely related to paracrystalline domains. Indeed, focusing on g-parameters exclusive may have led to conundrums and misinterpretations in the past. For example, based on the g-parameter value, some of the current champion polymers materials for organic solar cells (OSCs), namely poly[[4,8-bis[5-(2-ethylhexyl)-2-thienyl]benzo[1,2-*b*:4,5-*b*′]dithiophene-2,6-diyl]-2,5-thiophenediyl[5,7-bis(2-ethylhexyl)-4,8-dioxo-4*H*,8*H*-benzo[1,2-*c*:4,5-*c*′]dithiophene-1,3-diyl]] (PBDB-T), and its fluorinated (PBDB-T-2F or PM6) and chlorinated (PBDB-T-2Cl or PM7) derivatives (Fig. 2) have been classified as structurally amorphous.[15] Moreover, the absence of optical birefringence and measurable melting signals in DSC supported this conclusion. As a result, most advanced morphology-function models for OSC materials systems have been established on the premise that these polymers are structurally disordered.[16,17] However, distinctive aggregate-like domains are clearly revealed when these materials are inspected by electron or force microscopies, reflecting some sort of regional molecular packing.[8,18,19] Furthermore, this paradox seems not exclusive of OPV-related polymers, as the structural analysis of high-charge-mobility polymers, like indacenodithiophene-*co*-benzothiadiazole polymers (IDT-BT), has resulted in similar conundrums.[20–22] These seemingly contradictory results suggest that (i) g-parameter – alone – may not be adequately reflecting the overall structural order in these polymer materials, therefore (ii) the actual degree of structural order – and, hence, the overall solid-state microstructure – of many of the best-performing semiconducting polymers remains still unknown.

In this paper, we solve this apparent paradox by introducing a new concept: the degree of paracrystallinity. Analogously to the degree of crystallinity in semi-crystalline materials, the

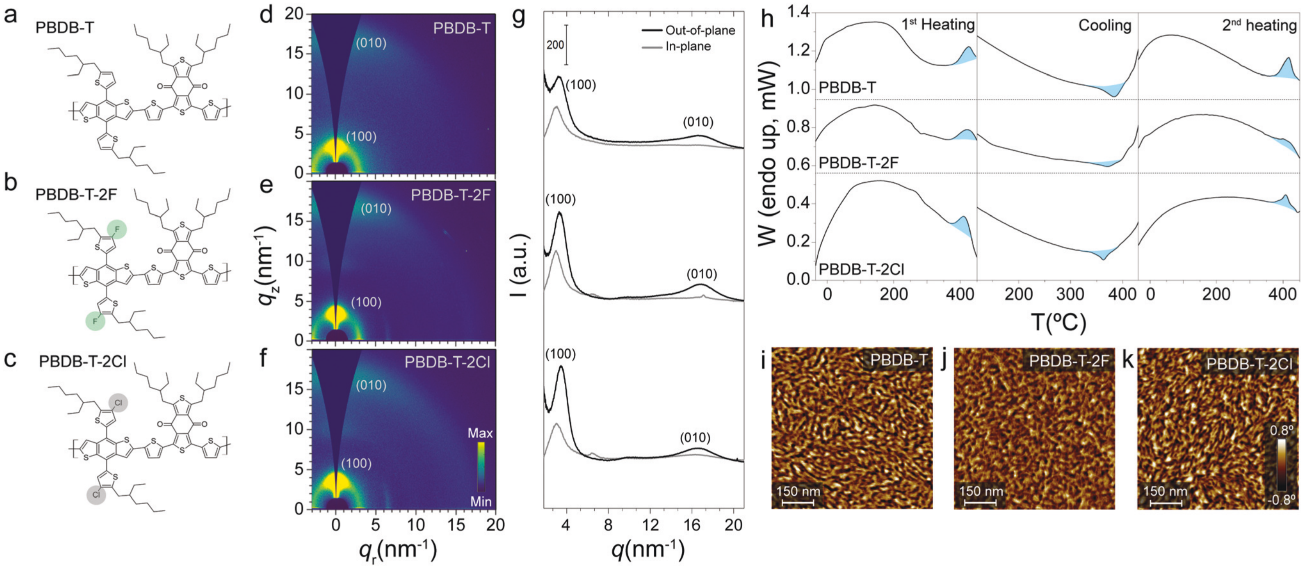

Fig. 2 Chemical structures of (a) PBDB-T, (b) PBDB-T-2F (PM6) and (c) PBDB-T-2Cl (PM7). 2D-GIWAXS pattern for spin-cast (d) PBDB-T, (e) PBDB-T-2F and (f) PBDB-T-2Cl. (g) Out-of-plane and in-plane GIWAXS profiles. (h) Representative fast scanning calorimetry (FSC) thermograms (raw data) for PBDB-T, PBDB-T-2F and PBDB-T-2Cl: 1st heating, cooling and 2nd heating scans are shown from left to right. Scanning rate was 4000 °C s^{-1} in all experiments. AFM phase-contrast images and for PBDB-T (i), PBDB-T-2F (j) and PBDB-T-2Cl (k), respectively.

degree of paracrystallinity features the mass/volume fraction of paracrystalline regions in semi-paracrystalline materials, without considering (in a first approximation) how ordered the molecular packing within paracrystalline domains is. Hence, the characterization of the overall structural order in rigid-backbone semi-conducting polymers would require two parameters: the *g*-parameter, which accounts for the lattice disorder within paracrystals, and the degree of paracrystallinity, which measures the mass/volume fraction of ordered material. The likely existing connection between both parameters needs to be investigated in future studies.

In addition to introducing this new concept, we propose that the degree of paracrystallinity of device-relevant thin films may be obtained from the melting enthalpy in fast scanning calorimetry (FSC) measurements. Hence, we demonstrate that, *e.g.* PBDB-T-2F, PBDB-T-2Cl and PBDB-T polymer films, which seem amorphous based on the *g*-parameter criteria, present notably high melting enthalpy values and thus they must be in fact notably ordered. The combination of this information with the characterization of nanomorphology and paracrystalline lattice distortion (*g*-parameter) provides a more reliable picture of the solid-state microstructure of these materials for the first time. We thus establish that a moderate-to-high degree of paracrystallinity in PBDB-T-2F, PBDB-T-2Cl and PBDB-T is underpinned by a highly dense arrangement of very small and very disordered paracrystalline domains. Having elucidated the semi-paracrystalline microstructure of polymer films, we investigate the interplay between the long-range charge transport and the structural features. Our data seem to demonstrate that the field-effect charge mobility is very sensitive to the presence of small paracrystallites interconnecting primary paracrystals.

Results and discussion

In full accordance with previous reports,[15] when standard procedures to assess the solid-state microstructure of polymeric materials are employed, results suggest that spin cast PBDB-T, PBDBT-2F and PBDBT-2Cl films are amorphous. For example, films are not birefringent under POM (see Fig. S1, ESI†); reliable endothermic peaks associated to crystal melting processes are not detected in DSC traces (likely because thermal degradation of polymers occur at lower temperature than melting peaks) (Fig. S2 of ESI†); and grazing incidence wide angle X-ray scattering (GIWAXS) patterns in Fig. 2d–f and profiles in Fig. 2g exhibit broad diffraction maxima from the π-stacked planes, *i.e.* the (010), and the lamellar packing of aromatic backbones and aliphatic side chains, *i.e.* the (100). The analysis of the (010) and (100) diffraction peaks disclose *g*-values between 16 and 19% and between 22 and 23%, respectively (Table 1), which are well-beyond those traditionally considered for structurally ordered materials (according to the standardized *g*-scale, ordered materials exhibit *g*-parameters between 0 and 12%).[23]

However, when identical spin-cast films are characterized by fast scanning calorimetry (FSC), intense endothermic signals are revealed at ~400 °C (as shown in panels labelled as "1st heating" in Fig. 2h), coinciding with the temperatures where (100) diffraction peaks disappear in temperature-resolved *in situ* grazing incidence X-ray scattering (GIWAXS) experiments (Fig. S3 of the ESI†) and the softening point of the polymer. Hence, these intense endothermic processes detected by calorimetry must be related to an order–disorder transition. In other words, these polymer films ought to exhibit some kind of solid-state structural order at room temperature, *i.e.*, they

Table 1 Peak parameters: peak position and paracrystallinity disorder parameter, *g*, values of the identified GIWAXS reflections in polymer films. *g* (%) was estimated with $g = \sqrt{\frac{\Delta q}{2\pi \cdot q_0}}$ being q_0 the maximum peak position and Δq the full width half maximum of the peak.[24] (Such analysis assumes that the peak width is dominated by disorder and not lattice parameter fluctuations or finite size)

		Lamellar (100)			(002)			π–π (010)		
Polymer	Microst.	q, nm^{-1} (d, nm)	L_c (nm)	g (%)	q, nm^{-1} (d, nm)	L_c (nm)	g (%)	q, nm^{-1} (d, nm)	L_c (nm)	g (%)
PBDB-T	A	3.4 (1.84)	5.8	22.6	—	—	—	16.9 (0.37)	1.8	18.1
	B	3.2 (1.93)	7.1	20.7	—	—	—	17.2 (0.36)	2.2	16.2
	C	3.2 (1.97)	11	16.9	—	—	—	17.2 (0.36)	2.8	14.4
PBDB-T-2F	A	3.4 (1.85)	5.3	23.5	6.6 (0.96)	11.2	11.7	17.0 (0.37)	2.2	16.5
	B	3.2 (1.93)	6.4	22.0	6.5 (0.97)	11.0	11.8	17.1 (0.37)	2.3	15.9
	C	3.2 (1.94)	10	17.5	6.5 (0.96)	11.6	11.5	17.1 (0.37)	2.6	14.9
PBDB-T-2Cl	A	3.5 (1.79)	5.4	23.0	6.4 (0.98)	11.6	11.6	16.8 (0.37)	1.6	19.1
	B	3.3 (1.88)	6.5	21.5	6.5 (0.97)	10.9	11.9	16.8 (0.37)	1.7	18.5
	C	3.4 (1.85)	13	15.1	6.5 (0.97)	13.3	10.7	17.0 (0.37)	2.2	16.2

ought to be – at least – paracrystalline. We note, moreover, that our data seems incompatible with such solid-state microstructure being a solidified liquid-crystal, as has been suggested. A solidified liquid crystal would become mechanically softer at temperatures much lower than that of the order–disorder transition, *i.e.*, at the T_g, which does not occur in the films. Moreover, the appearance of weak annealing-induced peaks in isothermal calorimetric experiments is more compatible with a solid-state order than with a liquid-crystalline-like order (Fig. S4 of the ESI†). We must note that the 1st heating scans shown in Fig. 2h reflect the thermal properties of the solid-state microstructure developed during the spin coating process. We also note that included in the Fig. S5 (ESI†) are a full set of experiments conducted in order to demonstrate that the endothermic signal detected is due to an order–disorder process and not due to degradation.

Importantly, a further outcome of these results is that GIWAXS and calorimetry seem to disagree when traditional definitions and *g*-parameter boundary benchmarks are used. Our data seems to suggest that the *g*-parameter scale based on a-SiO_2 reference may not be appropriate to classify semiconducting polymer thin films by their structural order, and a *g*-value higher than 12% needs to be established as the correct boundary benchmark for amorphous polymer semiconductors. But further interpretation is that the validity of the typically used GIWAXS-based *g*-parameter to evaluate the degree of order to paracrystalline domains needs to be questioned. GIWAXS provides a single *g*-parameter value for the entire sample volume, and thus it might encompass a contribution from both para-crystalline and disordered domains. Hence, disordered regions might be artificially increasing the *g*-value of paracrystalline domains in semi-paracrystalline materials. And, the higher the fraction of disordered domains in the sample – *i.e.* the lower the degree of paracrystallinity – the larger the resultant *g*-parameter (irrespectively of the actual degree of distortion of paracrystalline domains). We also note that determination of the *g*-parameter from a single peak makes the assumption that neither lattice parameter fluctuations nor finite size effect impact the peak width. If these assumptions are violated, the *g*-parameter is overestimated and use of GIWAXS assessment without complementary calorimetric data would be misleading.

Our calorimetric data revealed, moreover, that paracrystalline order–disorder transition is a reversible process. We deduce this from the FSC cooling sweeps of the three polymer films (conducted at 4000 °C s^{-1}), which display exothermic peaks at about 350 °C due to the formation of paracrystals upon cooling. This highlights that (a) paracrystals can be also formed by cooling the molten polymers and (b) that the formation of paracrystals is an extremely efficient and fast process, as paracrystals can be even formed during cooling at -4000 °C s^{-1} (we note that crystallization of polymers is most frequently suppressed at similar cooling rates even for highly crystalline flexible polymers like poly(ethylene oxide) (Fig. S6 in ESI†).

Both paracrystal melting and formation occurs at very high temperatures, which may seem surprising at a first glance but it can be rationalized with simple thermodynamic arguments: as in any first order phase transition, the change of free energy, ΔG, during paracrystal melting and formation must be equal to zero. Thus, $T_m\Delta S = \Delta H$ is fulfilled. ΔS is expected to have a reduced value because: (i) the structural order of the paracrystalline arrangement is rather low (*i.e.* high *g*-values); hence, paracrystallites are expected to have a high entropy. (ii) These polymers have a moderate-to-large persistent lengths (about 7 nm), and thus, the entropy of the melt is expected to be low. On the other hand, ΔH seems to be large, which would partially explain why we observe such large experimental melting enthalpies in FSC experiments. Therefore, being ΔS small and ΔH large, the transition temperature T_m must be commensurably high.

Interestingly, the enthalpy change during the melting of paracrystals formed from solution (probed in the 1st heating scan) and from the melt (probed in the 2nd heating scan) is different, which suggests that these two samples contain different fractions of paracrystalline domains (and amorphous domains), further confirming that significant fractions of disordered material exist together with the paracrystals. Therefore, the microstructure of these semiconducting polymers is not adequately represented by the standard paracrystalline model, which does not include discrete amorphous regions. In order to describe the microstructure of these polymer materials we introduce the concept of the semi-paracrystalline microstructure.

Because the enthalpy change during the order–disorder transition can be measured from the FSC scan, one should be able to quantitatively estimate a value of the fraction of paracrystalline material. By analogy with semicrystalline materials, we named this parameter the degree of paracrystallinity. The degree of paracrystallinity can potentially be obtained from FSC by normalizing the measured enthalpy to that of the 100% paracrystalline material.

However, this data is still unknown and hence should be elucidated for relevant semi-paracrystalline polymers. Moreover, we must note that the enthalpy of fusion of the 100% paracrystal should depend on the degree of order of the paracrystalline lattice, *i.e.* on the *g*-parameter, revealing a further link between the degree of paracrystallinity and *g*-parameter.

Hence, the characterization of the overall structural order in semi-paracrystalline materials would require two parameters: the *g*-parameter, which accounts for the lattice disorder within paracrystals, and the degree of paracrystallinity, which measures the mass/volume fraction of paracrystalline material.

The question arises as to how semi-paracrystalline microstructure looks like; and more specifically, how to conciliate the high degrees of paracrystallinity measured with the high *g*-values and the fact that materials are not birefringent. In order to shed light on this matter we investigated the morphology of the films in the length-scale of a few tens of nm by grazing incidence small angle X-ray scattering (GISAXS) and atomic force microscopy (AFM). GISAXS data (included in Fig. S11 of the ESI†) and, more clearly, the AFM phase-contrast images displayed in Fig. 2i–k, suggest a multiphasic nanomorphology that is compatible with the coexistence of very small paracrystalline domains separated by more disordered regions. Both power spectral density (PSD) (Fig. S12 of ESI†) analysis of the AFM images (shown in Fig. S13–S15 of the ESI†) and GISAXS analysis revealed an average characteristic structural length scale of 35–45 nm, which is most likely related to the spacing between clusters of paracrystallites, while paracrystallites seem to be much smaller than that. Indeed, the X-ray coherence length (L_c) values calculated (from GIWAXS) along lamellar packing (100), chain direction (020) and π-stack direction (010) were ∼6, ∼11 (PBDB-T-2Cl and PBDB-T-2F) and ∼2, respectively (Table 1). Hence, altogether, our data suggest that the semi-paracrystalline microstructure relies on the presence of a very dense arrangement of small paracrystallites, as shown schematically in Fig. 4a. Within these paracrystallites, molecular packing lacks of long-range order, along both the lamellar direction and the π-stacking direction. We note that although paracrystalline domains in our schematic in Fig. 4a include chain folding, we do not have experimental evidences of the occurrence of such phenomenon. We also note that the analysis of the (100) peak suggests the validity of the paracrystalline model for the molecular packing along that direction as well (Fig. S16 of the ESI†).

Motivated by our findings, we investigated whether other high-performing semi-conducting polymers and photovoltaic blends that, based primarily on X-ray diffraction data, have been so far considered poorly-ordered or amorphous, exhibit a semi-paracrystalline microstructure. Thus, D18 (a conjugated polymer containing dithieno[3′,2′:3,4;2″,3″:5,6]benzo[1,2-*c*][1,2,5]thiadiazole), PTB7 (poly[[4,8-bis[(2-ethylhexyl)oxy]benzo[1,2-*b*:4,5-*b*′]dithiophene-2,6-diyl][3-fluoro-2-[(2-ethylhexyl)carbonyl]thieno[3,4-*b*]thiophenediyl]]), a fluorobenzotriazole-based polymer (PBnDT-FTAZ),[25–27] and an IDT-BT,[28] as well as the binary blends PBDB-T : ITIC (1 : 1) and PBDB-T-2Cl : ITIC (1 : 1), were analyzed. For the sake of comparison, a well-known amorphous semi-conducting polymer, PTAA has been analyzed by FSC and the commodity semi-crystalline polymers PCL and PVDF,[5,29] and the semi-conducting polymer P3HT have been analyzed by GIWAXS. Molecular structures of the materials above are included in Fig. S17 of the ESI†).

D18, PTB7, PBnDT-FTAZ and IDT-BT films exhibited large *g*-values and low L_c values compared to common semi-crystalline polymers (data included in Table 2). In addition, contrarily to amorphous polymers like PTAA (data shown in Fig. 3b), FSC heating curves of the polymers above showed clear endothermic peaks (Fig. 3b). Altogether, these results suggest that many of the highest high-performing polymers for OSC and field effect transistors (FETs), such as D18, PTB7, PBnDT-FTAZ, IDT-BT, PM6, PBDB-T, *etc.* may exhibit a semi-paracrystalline microstructure (we note that a deeper analysis of IDT-BT films is included in the Fig. S18 of the ESI†).

Then, we endeavored to investigate whether this microstructure is retained in donor:acceptor blends like those employed in OSC devices. For that, we investigated a PBDB-T : ITIC (1 : 1) binary blend produced using similar processing conditions as those employed in efficient device preparation (*i.e.* spin casting a chlorobenzene solution containing 0.5% 1,8-diiodooctane, DIO, followed by a thermal annealing at 160 °C).[15] Like neat polymer films, bulk heterojunctions seem to be amorphous when they are characterized by GIWAXS (Fig. 3b). However, an endothermic feature showing up at about 400 °C in the FSC heating scan suggests the melting of PBDB-T para-crystals, revealing para-crystalline order also in donor domains of binary blends. Note: the endothermic peaks at about 200–260 °C are due to calorimetric signals from ITIC domains (*e.g.* the glass transition and the melting of crystalline phases).[30]

Table 2 Peak parameters for a variety of polymers. Paracrystallinity disorder parameter, *g*, calculated for the samples analyzed. *g* (%) was estimated with $g = \sqrt{\frac{\Delta q}{2\pi q_0}}$ being q_0 the maximum peak position and Δq the full width half maximum of the peak. L_c is calculated from $L_c = \frac{d_{hkl}}{2\pi g^2}$[1,24]

		Lamellar (100)			π–π peak		
		q, nm^{-1}	L_c (nm)	g (%)	q, nm^{-1}	L_c (nm)	g (%)
Polymer	D18	3.2	12.9	15.4	16.8	3.2	13.6
	PBnDT-FTAZ	3.4	4.9	24.1	16.6	1.5	20.1
	PTB7	—	—	—	16.8	1.7	18.6
	IDT-BT	3.8	12.1	14.8	14.9	1.5	21.0
	P3HT	2.8	10.2	18.6	16.8	7.0	9.3
	PCL	—	—	—	15.5[a]	161.1	4.4
	PVDF	—	—	—	19.0[a]	33.2	1.8
Blend	PBDB-T:ITIC	3.3	5.9	22.6	16.8	1.4	20.6
	PBDB-T-2Cl:ITIC	3.9	9.0	16.9	16.3	3.3	13.6

[a] PCL and PVDF do no exhibit a π–π peak, hence, their main diffraction peak has been included in the table.

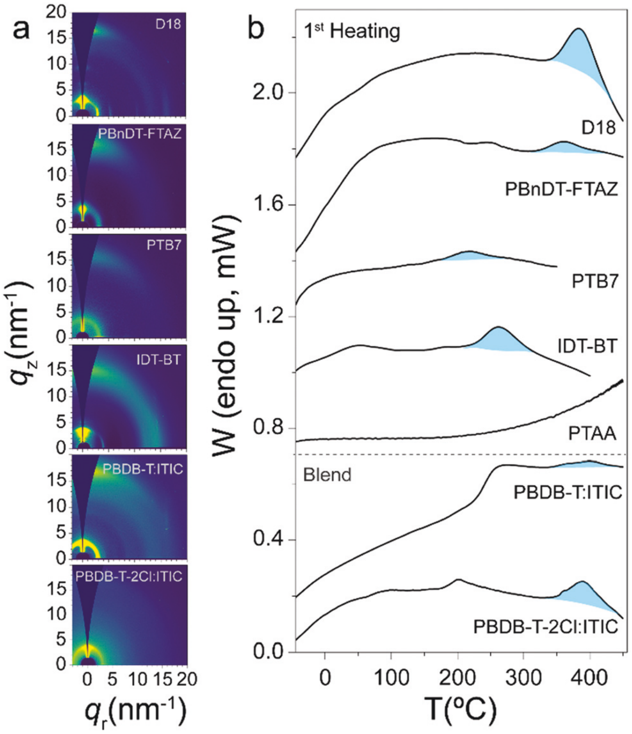

Fig. 3 GIWAXS patterns (a) and FSC heating traces (b) for a variety of polymers (D18, PBnDT-FTAZ, PTB7, IDT-BT, PTAA) and photovoltaic blends (PBDB-T:ITIC and PBDB-T-2Cl:ITIC).

Although the detailed interplay between thermal and diffraction characterization has to be more explored and understood, we can identify some common experimental signatures of the semi-paracrystalline organization: as opposed to semicrystalline materials, semi-paracrystalline materials seem to exhibit *g*-parameters comparable to those of amorphous materials (frequently >15), L_c values in the range of 1–3 nm and they are non-birefringent; as opposed to amorphous materials they exhibit order–disorder transitions that are visible by calorimetry. A further question that needs to be answered in future works is to what extent, this definition of L_c, which has been often used in the past,[1,24,31] is applicable to materials exhibiting a semi-paracrystalline organization. The calculation of L_c assumes that the loss of X-ray coherence is solely due to cumulative lattice disorder, *i.e.* the material is considered to be infinite paracrystal. However, the semi-paracrystalline framework establishes that paracrystalline domains are finite – indeed, rather small- and have boundaries, which introduce likely abrupt lattice parameter changes. Hence, the breath of the diffraction peak might result from -at least- two mechanisms: paracrystalline disorder and the finite-size of paracrystalline domains.

As other multiphasic solid-state microstructures of polymer materials, *e.g.*, the semicrystalline organization, the semi-paracrystalline microstructure is sensitive to temperature (Fig. 4). Hence, in a first approximation, the interplay between the characteristic features of the semi-paracrystalline microstructure and electronic properties can be investigated by analyzing the charge carrier mobility, μ, of semi-paracrystalline films annealed at various temperatures (Fig. 5). We would like to note that, despite the main application of the polymers analyzed here is OPV, we refrained from making correlations between structural features of the semi-paracrystalline model and OSC device performances as the latter are also dictated by the structural characteristics of the acceptor and the blend morphology and both change dramatically when the thermal protocols required to induce modifications of the semi-paracrystalline organization are applied.

Here, we will base our discussion on the results obtained for PBDB-T-2Cl, which is shown in Fig. 4, while the corresponding results for the rest of polymers are included in Fig. S19–S22 (ESI†). GIWAXS (Fig. 4d–h and Table 1), UV-vis spectroscopy (Fig. S23 of the ESI†) and AFM (Fig. 4j and k) results show little differences in *g*-parameter and nanomorphology between the as-cast A-microstructure and that of the material after being annealed at intermediate temperatures (*e.g.* 160 °C for PBDB-T-2Cl), which is denoted here as B-microstructure. However, the FSC trace of B-microstructure, in Fig. 4i, exhibits a new endothermic peak between 200 and 300 °C. We associate this peak with the melting of new paracrystallites that develop during the annealing step at temperatures above the T_g.[32] According to their low melting temperatures, these new paracrystallites must be even smaller and/or more defective than the preexisting ones.

From the measurement of their melting enthalpies, we deduce that the development of these paracrystallites results in a minor increase of the overall degree of paracrystallinity. Moreover, because no changes are observed in the melting peaks of preexisting paracrystals, we rule out a significant secondary paracrystallization and paracrystal perfectioning processes during the thermal annealing in this temperature range. Interestingly, despite of the minor structural differences between microstructures-A and -B, we found that microstructure-B exhibits a 2.5-to-4-times higher μ-value than microstructure-A in these polymers (Fig. 5b). We argue that this improvement of charge transport results from the fact that the new paracrystals grow in disordered regions in between preexisting paracrystals, and thus they enhance interconnection pathways between structurally ordered units, similarly to the charge transport model by Noriega and Salleo.[1] Raw transistor data are included in Fig. 5a and in Fig. S24 (ESI†).

The semi-paracrystalline microstructure changes substantially, however, when it is thermally annealed at higher-temperatures (the resulting solid-state microstructure is named here as C-microstructure). FSC curves for C-microstructure, shown in Fig. 4i, reveal larger melting enthalpies. The increase of the melting enthalpy (ΔH_f) for each specific polymer system as a result of the annealing is connected with the annealing-induced relative increase of the degree of paracrystallinity in that sample (ΔX_c). Thus, ΔH_f of paracrystalline domains increase from 16.2 ± 1.4 J g^{-1} to 23.6 ± 1.6 J g^{-1} (a 45% increase of ΔX_c) for PBDB-T and from 34.9 ± 3.3 J g^{-1} to 43.9 ± 1.4 J g^{-1} (a 25% increase of ΔX_c) for PBDB-T-2Cl (Fig. 5c). The value for PBDB-T-2F could not be extracted from our data as the melting peak shifted out of the

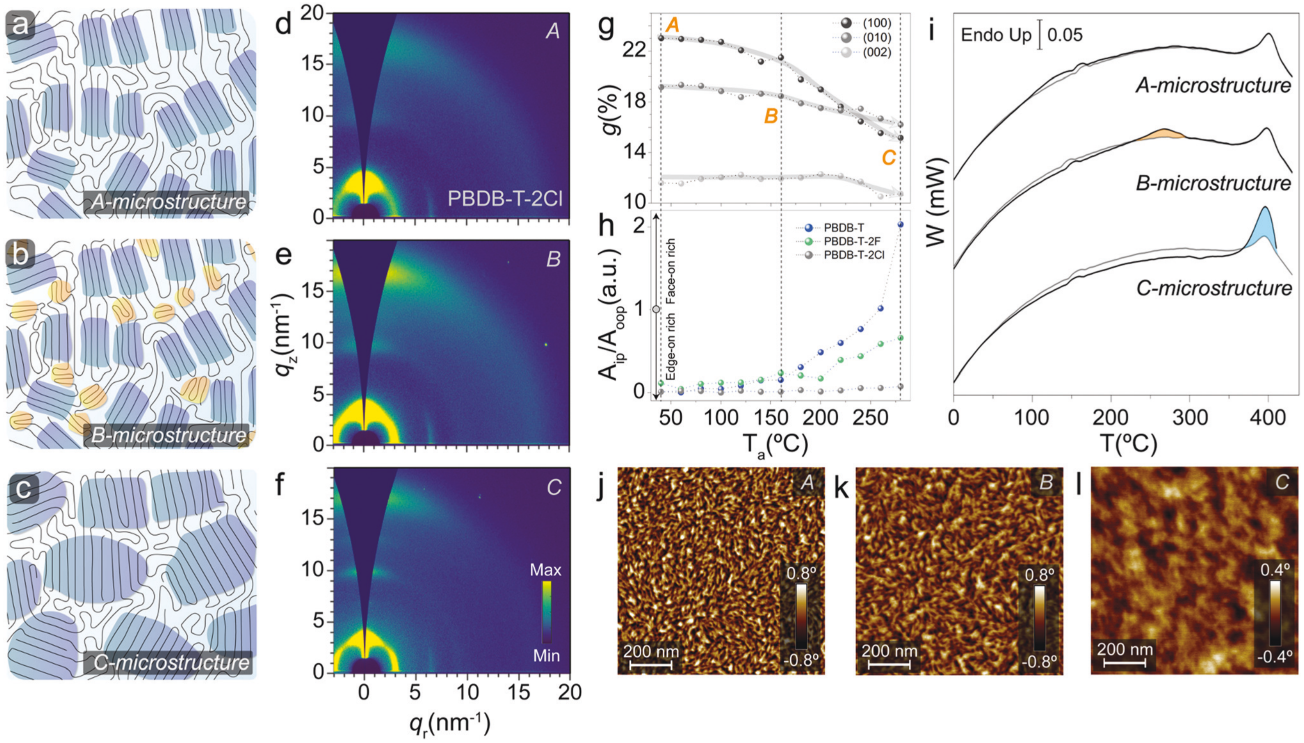

Fig. 4 Evolution of the semi-paracrystalline microstructural organization with temperature. Schematics depicting the so-called A- (a), B- (b) and C-microstructures (c) in a semi-paracrystalline polymer material. *Ex situ* 2D-GIWAXS patterns for PBDB-T-2Cl in the A- (d), B- (e) and C-microstructures (f). (g) Paracrystalline distortion parameter, *g*, for the (100), (010) and (002) planes as a function of the annealing temperature, T_a, for PBDB-T-2Cl. (h) Ratio between the (100) diffraction maxima along the in-plane and the out-of-plane directions (A_{ip}/A_{oop}) as a function of T_a, for PBDB-T-2Cl. (i) Fast scanning calorimetry thermograms (raw data) of PBDB-T-2Cl A- (annealed at 60 °C), B- (annealed at 160 °C) and C-microstructures (annealed at 280 °C): thick black lines correspond to heating scans after films were cooled down from the melt at 4000 °C s^{-1} to the selected annealing temperature followed by a 2 h annealing at that temperature, while grey lines correspond to heating scans of non-annealed films. Atomic force microscopy phase images for PBDB-T-2Cl A- (j), B- (k) and C-microstructures (l).

available experimental window). This increase of the degree of paracrystallinity coincides with a significant enlargement of the paracrystals, as deduced from the AFM analysis included in Fig. 4l (and in Fig. S25–S28 of the ESI†) as well as the increase of the L_c-value of lamellar packing, (100), from 5–7 to 10–13 (see Table 1). Furthermore, the *g*-values for the (100) and (010) planes are significantly lower in C-microstructures (see Fig. 4g and Table 1), reflecting a reduction of the lattice disorder of paracrystalline domains. In contrast, temperature seems to have a little impact on molecular conformation and short-range molecular arrangement, as probed by UV-vis spectroscopy (results shown in Fig. S23 of the ESI†).

The apparent increase of the degree of paracrystallinity, the larger paracrystalline domains and the reduction of lattice distortion can explain the larger μ-values of C-microstructures in PBDB-T-2F and PBDB-T-2Cl compared to B-microstructures (Fig. 5c and d). Interestingly, the opposite trend is found for PBDB-T (Fig. 5e). The texture analysis for this polymer, shown in Fig. 4h (A_{ip}/A_{oop} refers to the ratio between the areas of the (100) diffraction peaks along the out-of-plane and the in-plane directions), highlights that PBDB-T paracrystals suffer from a progressive change of orientation as the T_a increases, yielding a preferential face-on orientation at the higher T_as analyzed, *i.e.* those leading to C-microstructures. Face-on oriented paracrystals have their (010) planes parallel to the substrate, which may hinder the in-plane charge transport probed in our devices, resulting in the low mobility observed for the PBDB-T C-microstructure. It can be concluded, however, that the combined impact of the increase of the degree of paracrystallinity, the decrease of the lattice disorder and the enhancement of the paracrystallite interconnection on the charge transport seems to be greater than that of the paracrystal orientation, because C-microstructure exhibits higher μ than A-microstructure even for PBDB-T.

Conclusions

We introduce a new model to describe structural order in high-performing, rigid semi-conducting polymers, such as the PBDB-T family, IDT-BT, PTB7 or PBnDT-FTAZ. Employing fast scanning calorimetry, we discover that these materials can be notably ordered. The prior conundrum about whether or not these polymers are structurally ordered or amorphous originates from employing the *g*-parameter as the only criteria to assess structural order. These materials often exhibit *g*-parameter values that are similar to those of amorphous a-SiO_2, which can lead to mistakenly interpret that these materials are amorphous. Though paracrystalline lattices are indeed largely distorted in these

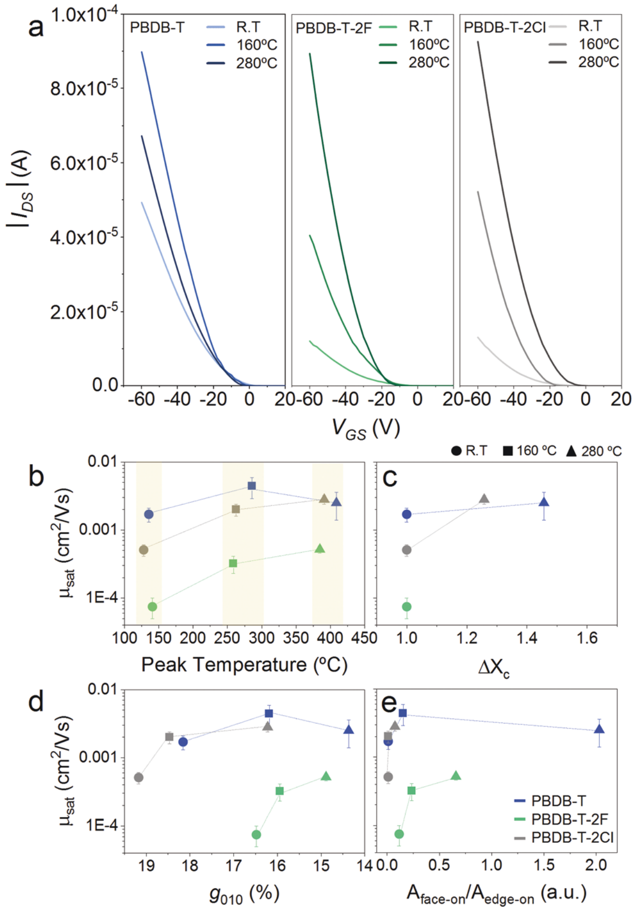

Fig. 5 Representative transfer characteristics for (a) PBDB-T, PBDB-T-2F and PBDB-T-2Cl field-effect transistors annealed at 25 °C, 160 °C and 280 °C. All transfer characteristics were measured in transistors with width W = 10 000 μm and length L = 40 μm. (b) Field-effect mobility, μ, for the different polymer samples plotted *vs.* the endothermic peak temperature (for A-microstructures, the broad endothermic signal appearing between 100 and 200 °C is considered, while for B- and C-microstructures the endothermic peak derived from the isothermal annealing step is considered). (c–e) μ *vs.* various structural characteristics: (c) μ *vs.* the relative increase of the degree of paracrystallinity obtained from melting enthalpy of paracrystalline domains (ΔH_f) ($\Delta X_c = (\Delta H_{f\,\text{after annealing}})/(\Delta H_{f\,\text{before annealing}})$); (d) μ *vs.* lattice distortion parameter of the π–π stack, g_{010}; and (e) μ *vs.* the ratio between the area of the (100) peak along the in-plane and the out-of-plane directions, A_{ip}/A_{oop}.

materials (even if the *g*-parameter might be overestimated), we find through calorimetry methods that some of these polymer materials seemingly contain large fractions of ordered material. Thus, we conclude that the precise assessment of structural order in rigid semiconducting polymers requires information about-at least-two parameters: the *g*-parameter, which accounts for the paracrystalline lattice distortion, and the degree of paracrystallinity (introduced here for the first time), which measures the mass/volume fraction of paracrystalline material from the analysis of order–disorder peaks in FSC scans. For that, the enthalpy of fusion of the 100% paracrystalline material needs to be measured-taking into account that this value should also depend to the *g*-parameter of the paracrystalline lattice. Indeed, the actual relationship between the degree of paracrystallinity and the *g*-parameter needs to be further analyzed in future studies and critically evaluated.

We demonstrate that the degree of structural order in the semi-paracrystalline polymers studied here is underpinned by a dense arrangement of very small and disordered paracrystallites that coexist with more disordered regions. The disordered fractions of semi-paracrystalline materials are reasonably expected to exhibit a glass transition process. This too needs to be researched.

A further open question that needs to answered is to what extend the semi-paracrystalline organization depends on film processing route; *e.g.* on deposition method, concentration, solvent used, *etc.*, as these influence phenomena such as chain aggregation and chain orientation that seem to be connected with the paracrystalline structures.

Partially in line with the charge transport model of semi-crystalline polymers by Noriega, Rivnay and Salleo,[1] the field-effect charge mobility of semi-paracrystalline polymer materials is especially sensitive to the interconnection of paracrystalline domains. The paracrystalline lattice disorder, the degree of paracrystallinity and the paracrystallite's size and orientation are also proven to impact charge transport. Because the semi-paracrystalline microstructure can be a common feature among many polymers having semi-rigid backbones and likely some amphiphilicity, we believe that our results can have direct implications not only in the organic electronics arena, where *e.g.*, device operation models must now include the degree of paracrystallinity, but also in other now seemingly unconnected applications and fields that use structurally similarly complex materials.

Methods

Materials

The polymer donors PBDB-T, PBDB-T-2F, PBDB-T-2Cl and PTB7 were supplied by Ossila Ltd. FTAZ was synthesized as previously reported. Chlorobenzene (CB) and chloroform ($CHCl_3$) were purchased from Merck and used as received.[33] Unless indicated, PBDB-T and PBDB-T-2Cl were spin cast from 20 mg mL^{-1} chlorobenzene solutions at 2000 rpm during 60 s and PBDB-T-2F was spin cast from 16 mg mL^{-1} chloroform solutions at 3000 rpm. PBDB-T : ITIC (1 : 1) and PBDB-T-2Cl : ITIC (1 : 1) binary blend produced using similar processing conditions as those employed in efficient device preparation (*i.e.* spin casting a chlorobenzene solution containing 0.5% 1,8-diiodooctane, DIO, followed by a thermal annealing at 160 °C).[34]

Fast scanning calorimetry (FSC)

FSC measurements were carried out in a Mettler Toledo Flash DSC 1 equipped with a two-stage intracooler, allowing for temperature control between −90 and 450 °C and nitrogen purge (75 mL min^{-1} N_2 gas flow). MultiSTAR UFS1 (24 × 24 × 0.6 mm^3) MEMS chip sensors were conditioned and corrected according the specifications prior to use. For the experiments, polymer solutions were spin cast onto the backside of the chip sensor. For analysis of the 1st heating scan of spin coated films, samples were scanned between −90 °C and 450 °C at 4000 °C s^{-1}. 2nd heating scans were obtained in the same experimental conditions after the film were cooled down from 450 °C to −90 °C at 4000 °C s^{-1}. We selected 4000 °C s^{-1} for the heating scans because this scanning rate allows an excellent compromise for obtaining high signal intensities, resulting in low thermal lag and avoiding thermal degradation of samples as well as secondary crystallization[35] (see S5 of the ESI†).

To calculate melting enthalpy of paracrystalline domains (ΔH_f) the heat flow-rate signal directly obtained from FSC experiments is transformed into heat capacity (c_p) units with the calculated mass and the heating rate [c_p (J °C^{-1} g^{-1}) = (W (J s^{-1}))/(m (g) β (°C s^{-1}), where c_p, W, m and β and specific heating capacity, heat flow-rate, mass and heating rate]. Sample mass is obtained from sample volume using the density value of P3HT (1.1 g cm^{-3}).[36] Volume of investigated samples is calculated as the chip area is known and the film thickness is measured by profilometry. Errors in the measurement of ΔH_f consider (i) the possibility of delineating a number of different peak baselines (Fig. S31 of the ESI† and (ii) standard deviation of the film thickness values obtained from profilometry. However, a further error is likely introduced in the integration of some melting peaks due to the fact that by the fact that some melting peaks seem not to be completely resolved in the high-temperature-side.

Grazing incidence wide angle X-ray scattering (GIWAXS)

GIWAXS measurements were performed at the BL11 NCD-SWEET beamline at ALBA Synchrotron Radiation Facility (Spain). The incident X-ray beam energy was set to 12.4 eV using a channel cut Si (1 1 1) monochromator. The angle of incidence α_i was set between 0.1–0.15° to ensure surface sensitivity. We note that larger incident angles have been also investigated in order to ensure that we probe the bulk of the film and not just the surface (Fig. S29 and S30, ESI†). The scattering patterns were recorded using a Rayonix® LX255-HS area detector, which consists of a pixel array of 1920 × 5760 pixels ($H \times V$) with a pixel size of 44 × 44 μm^2. Data are expressed as a function of the scattering vector (Q), which was calibrated using Cr_2O_3 as standard sample, obtaining a sample to detector distance of 200.93 mm. Temperature-resolved *in situ* X-ray experiments were performed using a Linkam® THMS 600 stage adapted for grazing incidence experiments. The heating rate used was 20 °C min^{-1} and the temperature difference between frames was 4 °C. Sample alignment was automatically performed each 50 °C. Exposure times for *in situ* and *ex situ* experiments were 1 and 5 s, respectively. All the measurements were performed under N_2 atmosphere to minimize the damage of the films. 2D GIWAXS patterns were corrected as a function of the components of the scattering vector. Samples for GIWAXS were spin cast on Si wafers. The thermal treatments were performed in a Linkam hot stage under N_2 atmosphere. Edges of the samples were removed to eliminate edge effects in the GIWAXS pattern.

Grazing incidence X-ray scattering (GISAXS)

The GISAXS experiments were conducted at NCD-SWEET beamline of ALBA synchrotron (Spain). A monochromatic X-ray beam with an energy of 12.4 keV was shone on the samples with an incidence angle of 0.12° and 0.15°. We note that larger incident angles have been also investigated in order to ensure that we probe the bulk of the film and not just the surface (Fig. S29 and S30, ESI†). The exposure time for room temperature measurements was 1 s and the sample to detector distance was 2.54 m. The 2D patterns were recorded with a Pilatus3 S 1 M detector, which consists of a pixel array 1043 × 981 ($V \times H$) pixels of 172 × 172 μm^2. Horizontal line q_y cut profiles were done at the Yoneda peak. For GISAXS experiments samples were spin cast on Si wafers. The thermal treatments were performed in a Linkam hot stage under N_2 atmosphere. Edges of the samples were removed to eliminate edge effects in the GISAXS scattering pattern.

Atomic force microscopy (AFM)

AFM images were obtained using a scanning probe microscope (Dimension ICON, Bruker) under ambient conditions. Tapping mode was employed in air using an integrated tip/cantilever (125 μm in length with *ca.* 300 kHz resonant frequency). Scan rates ranged from 0.7 to 1.2 Hz s^{-1}. Measurements were performed with 512 scan lines and target amplitude around 0.9 V. The amplitude setpoint for all investigated samples was ~300 mV. Different regions of the samples were scanned to ensure that the morphology of the investigated materials is the representative one. In the AFM, phase images, the brighter regions correspond to areas of the sample with higher modulus (hard domains) and darker regions correspond to softer areas. Samples were spin cast from 20 mg mL^{-1} solution at 2000 rpm during 60 s. The thermal treatments were performed in a Linkam hot stage under N_2 atmosphere. Samples were annealed for 10 minutes at selected temperature and quenched at 50 °C min^{-1} to room temperature.

Quantitative information about the paracrystallite size was obtained from power spectral density (PSD) analysis applied on the AFM phase-contrast images using the NanoScope Analyses 1.9 software.

UV-vis spectroscopy

UV-vis spectra were recorded with a Shimadzu UV-2550 spectrometer with a film adapter. Samples were spin cast on glass slides and thermal treatments were performed in a Linkam hot stage under N_2 atmosphere.

Field-effect transistor fabrication and measurement

Field-effect transistors in a bottom gate, bottom contact geometry were fabricated by spin coating the different polymers onto Si/SiO_2 (150 nm) substrates with prepatterned pairs of Ti/Au (5 nm/36 nm) electrodes. The n++ Si substrate was used as gate electrode, the SiO_2 (150 nm) as gate dielectric and the Ti/Au contacts as source (S) and drain (D). The prepatterned pairs of electrodes with interdigitated geometry were fabricated using conventional lithographic techniques. Channel length (L) and widths (W) varied in the range $L \sim$ 5–50 μm and $W \sim$ 5000–10 000 μm.

The individual chips were cleaned with acetone and later with isopropanol. Before spin coating the polymers the chip were introduced in the ozone cleaner (supplied by Ossila Ltd) for 1 h. Samples were spin cast from 10 mg mL^{-1} solution at 2000 rpm during 60 s. The thermal treatments were performed in a Linkam hot stage under N_2 atmosphere. Samples were annealed for 10 minutes at selected temperature and quenched at 50 °C min^{-1} to room temperature.

The electrical characteristics of the transistors were measured using a Keithley 4200-SCS semiconductor analyzer connected to a variable temperature Lakeshore probe station. The measurements were carried out with the samples in high vacuum, and the samples were left 12 hours in vacuum prior to the measurements, to minimize the effect of oxygen doping.

To extract the field-effect mobility, the transfer curves were analyzed using standard field-effect transistor equations for the saturation regime:

$$I_{\mathrm{DS}} = -\frac{W}{2L}\mu C(V_{\mathrm{GS}} - V_{\mathrm{Th}})^2 \tag{1}$$

where I_{DS} is the drains source current, μ is the mobility, C is the capacitance per unit area, V_{GS} is the gate-source voltage and V_{Th} is the threshold voltage. In each chip, more than 10 devices were tested to extract the average mobility, and the error is given by the standard deviation.

Author contributions

The manuscript was written through contributions of all authors. All authors have given approval to the final version of the manuscript.

Conflicts of interest

There are no conflicts to declare.

Acknowledgements

S. Marina is grateful to POLYMAT for her PhD scholarship. J. M. thanks MICINN/FEDER for the Ramón y Cajal contract and the grant Ref. PGC2018-094620-A-I00). J. M. thanks support from Xunta de Galicia ED431F 2021/09 The Basque Country Government is also acknowledged for the grant Ref. PIBA19-0051. J. M. and E. F.-G. acknowledge support through the European Union's Horizon 2020 research and innovation program, H2020-FETOPEN-01-2018-2020 (FET-Open Challenging Current Thinking), 'LION-HEARTED', grant agreement no. 828984. J. M. would like to thank the financial support provided by the IONBIKE RISE project. This project has received funding from the European Union's Horizon 2020 research and innovation programme under the Marie Skłodowska-Curie grant agreement no. 823989. HA is supported by a Goodnight Innovation Distinguished Professor Endowment. J. J. R. and W. Y. acknowledge the financial support of the National Science Foundation (CBET-1934374). The authors thank Marek Grzelczak and Joscha Kruse for their support with UV-Vis spectroscopy measurements. The authors also thank the technical and human support provided by SGIker of UPV/EHU and the European funding (ERDF and ESF). The work at CIC nanoGUNE was supported by "la Caixa" Foundation (ID 100010434), under the agreement LCF/BQ/PI19/11690017 and by the Spanish MICINN under the Maria de Maeztu Units of Excellence Programme (MDM-2016-0618) and Project RTI2018-094861-B-100 and PID2019-108153GA-I00.

Notes and references

1 R. Noriega, J. Rivnay, K. Vandewal, F. P. V. Koch, N. Stingelin, P. Smith, M. F. Toney and A. Salleo, *Nat. Mater.*, 2013, **12**, 1038.

2 G. Strobl, *The Physics of Polymers: conceps for understanding their structures and behaviour*, Springer, Berlin Heidelberg New York, 3rd edn, 2007.

3 K. Hermann, O. Gerngross and W. Abitz, *Z. Phys. Chem. B*, 1930, **10**, 371.

4 F. Van Antwerpen and D. W. Van Krevelen, *J. Polym. Sci., Polym. Phys. Ed.*, 1972, **10**, 2409–2421.

5 J. Martín, A. Iturrospe, A. Cavallaro, A. Arbe, N. Stingelin, T. A. Ezquerra, C. Mijangos and A. Nogales, *Chem. Mater.*, 2017, **29**, 3515–3525.

6 M. G. Dobb, D. J. Johnson and B. P. Saville, *J. Polym. Sci., Polym. Phys. Ed.*, 1977, **15**, 2201–2211.

7 E. E. Magat, W. Watt, B. Harris and A. C. Ham, *Philos. Trans. R. Soc., A*, 1980, **294**, 463–472.

8 D. Qian, L. Ye, M. Zhang, Y. Liang, L. Li, Y. Huang, X. Guo, S. Zhang, Z. A. Tan and J. Hou, *Macromolecules*, 2012, **45**, 9611–9617.

9 D. W. V. Krevelen and K. T. Nijenhuis, *Properties of Polymers*, Elsevier Science, 2009.

10 R. Hosemann, *Polymer*, 1962, **3**, 349–392.

11 O. Zapata-Arteaga, A. Perevedentsev, S. Marina, J. Martin, J. S. Reparaz and M. Campoy-Quiles, *ACS Energy Lett.*, 2020, **5**, 2972–2978.

12 C. R. Snyder, R. C. Nieuwendaal, D. M. DeLongchamp, C. K. Luscombe, P. Sista and S. D. Boyd, *Macromolecules*, 2014, **47**, 3942–3950.

13 J. Balko, R. H. Lohwasser, M. Sommer, M. Thelakkat and T. Thurn-Albrecht, *Macromolecules*, 2013, **46**, 9642–9651.

14 J. Rivnay, R. Noriega, R. J. Kline, A. Salleo and M. F. Toney, *Phys. Rev. B: Condens. Matter Mater. Phys.*, 2011, **84**, 045203.

15 L. Yu, D. Qian, S. Marina, F. A. A. Nugroho, A. Sharma, S. Hultmark, A. I. Hofmann, R. Kroon, J. Benduhn, D.-M. Smilgies, K. Vandewal, M. R. Andersson, C. Langhammer, J. Martín, F. Gao and C. Müller, *ACS Appl. Mater. Interfaces*, 2019, **11**, 21766–21774.

16 M. Ghasemi, N. Balar, Z. Peng, H. Hu, Y. Qin, T. Kim, J. J. Rech, M. Bidwell, W. Mask, I. McCulloch, W. You, A. Amassian, C. Risko, B. T. O'Connor and H. Ade, *Nat. Mater.*, 2021, **20**, 525.

17 L. Ye, H. Hu, M. Ghasemi, T. Wang, B. A. Collins, J.-H. Kim, K. Jiang, J. H. Carpenter, H. Li, Z. Li, T. McAfee, J. Zhao, X. Chen, J. L. Y. Lai, T. Ma, J.-L. Bredas, H. Yan and H. Ade, *Nat. Mater.*, 2018, **17**, 253.

18 S. Zhang, Y. Qin, J. Zhu and J. Hou, *Adv. Mater.*, 2018, **30**, 1800868.

19 W. Köntges, P. Perkhun, J. Kammerer, R. Alkarsifi, U. Würfel, O. Margeat, C. Videlot-Ackermann, J.-J. Simon, R. R. Schröder, J. Ackermann and M. Pfannmöller, *Energy Environ. Sci.*, 2020, **13**, 1259–1268.

20 D. Venkateshvaran, M. Nikolka, A. Sadhanala, V. Lemaur, M. Zelazny, M. Kepa, M. Hurhangee, A. J. Kronemeijer, V. Pecunia, I. Nasrallah, I. Romanov, K. Broch, I. McCulloch, D. Emin, Y. Olivier, J. Cornil, D. Beljonne and H. Sirringhaus, *Nature*, 2014, **515**, 384–388.

21 C. Cendra, L. Balhorn, W. Zhang, K. O'Hara, K. Bruening, C. J. Tassone, H.-G. Steinrück, M. Liang, M. F. Toney, I. McCulloch, M. L. Chabinyc, A. Salleo and C. J. Takacs, 2021, arXiv:2104.13984v1.

22 Y. Cho, S. Park, S. Jeong, H. Yang, B. Lee, S. M. Lee, B. H. Lee and C. Yang, *J. Mater. Chem. C*, 2021, **9**, 9670.

23 C. R. Snyder and D. M. DeLongchamp, *Curr. Opin. Solid State Mater. Sci.*, 2018, **22**, 41–48.

24 J. Rivnay, R. Noriega, R. J. Kline, A. Salleo and M. F. Toney, *Phys. Rev. B: Condens. Matter Mater. Phys.*, 2011, **84**, 045203.

25 B. A. Collins, Z. Li, J. R. Tumbleston, E. Gann, C. R. McNeill and H. Ade, *Adv. Energy Mater.*, 2013, **3**, 65–74.

26 H. Hu, M. Ghasemi, Z. Peng, J. Zhang, J. J. Rech, W. You, H. Yan and H. Ade, *Adv. Mater.*, 2021, 2005348.

27 D. He, F. Zhao, J. Xin, J. J. Rech, Z. Wei, W. Ma, W. You, B. Li, L. Jiang, Y. Li and C. Wang, *Adv. Energy Mater.*, 2018, **8**, 1802050.

28 W. Zhang, J. Smith, S. E. Watkins, R. Gysel, M. McGehee, A. Salleo, J. Kirkpatrick, S. Ashraf, T. Anthopoulos, M. Heeney and I. McCulloch, *J. Am. Chem. Soc.*, 2010, **132**, 11437–11439.

29 J. Martin, D. Zhao, T. Lenz, I. Katsouras, D. de Leeuw and N. Stingelin, *Mater. Horiz.*, 2017, **4**, 408.

30 S. Marina, A. D. Scaccabarozzi, E. Gutierrez-Fernandez, E. Solano, A. Khirbat, L. Ciammaruchi, A. Iturrospe, A. Balzer, L. Yu, E. Gabirondo, X. Monnier, H. Sardon, T. D. Anthopoulos, M. Caironi, M. Campoy-Quiles, C. Müller, D. Cangialosi, N. Stingelin and J. Martin, *Adv. Funct. Mater.*, 2021, **31**, 2103784.

31 A. Luzio, J. Martin, C. H. Cheng, N. Stingelin, M. F. Toney, A. Salleo and M. Caironi, *J. Mater. Chem. C*, 2021, **9**, 15848–15857.

32 C. Schick and R. Androsch, *Macromolecules*, 2020, **53**, 8751–8756.

33 Q. Zhang, L. Yan, X. Jiao, Z. Peng, S. Liu, J. J. Rech, E. Klump, H. Ade, F. So and W. You, *Chem. Mater.*, 2017, **29**, 5990–6002.

34 W. Zhao, D. Qian, S. Zhang, S. Li, O. Inganäs, F. Gao and J. Hou, *Adv. Mater.*, 2016, **28**, 4734–4739.

35 A. Luzio, F. Nübling, J. Martin, D. Fazzi, P. Selter, E. Gann, C. R. McNeill, M. Brinkmann, M. R. Hansen, N. Stingelin, M. Sommer and M. Caironi, *Nat. Commun.*, 2019, **10**, 3365.

36 https://scholarsphere.psu.edu/resources/1f0cd735-6a0d-4c6d-aaea-17369594db0c.